Science Arts & Métiers (SAM)

To cite this version :

Multiaxial high cycle fatigue damage mechanisms associated with the different microstructural heterogeneities of cast aluminium alloys

Viet-Duc Le [a,b,c,*], Franck Morel [a], Daniel Bellett [a], Nicolas Saintier [b], Pierre Osmond [c]

[a] Arts et Métiers ParisTech, CER Angers – Laboratoire LAMPA – 2 Bd du Ronceray, 49035 Angers Cedex 1, France
[b] Arts et Métiers ParisTech, CER Bordeaux – Laboratoire I2M – Esplanade des Arts et Métiers, 33405 TALENCE Cedex, France
[c] PSA Peugeot Citroën, 18 rue des fauvelles, 92256 La Garenne-Colombes cedex, France

ABSTRACT

This paper is dedicated to the high cycle fatigue (HCF) behaviour of cast Al–Si alloys. In particular, three similar alloys with different microstructural characteristics are investigated. The result of an experimental campaign is presented, in order to characterise the fatigue behaviour, and more specifically the fatigue damage mechanisms related to the different microstructural heterogeneities (i.e. casting porosity, dendrite size, SDAS, non-metallic inclusions and silicon particles), observed under different multiaxial loading conditions: pure tension, plane bending, pure torsion and combined tension–torsion with a load ratio $R = -1$.

It is shown that casting porosity has a very detrimental influence on the uniaxial and combined tension–torsion fatigue strengths. However, a much lower influence is observed for the torsional fatigue strength.

For the porosity-free alloy, it is observed that the formation of persistent slip bands (PSB) in the aluminium matrix is the major fatigue crack initiation mechanism regardless of the loading modes, at a load ratio of $R = -1$. It is also shown that the aluminium matrix has a large role in the formation of PSB and that the Si particles facilitate the formation of PSB.

1. Introduction

Automotive manufacturers have the choice of several casting processes and post-casting heat treatments for the fabrication of cast aluminium components, such as cylinder heads, used in their vehicles. Typical casting processes include gravity die casting and lost foam casting (LFC) and the components are subsequently heat treated via standard T6 or T7 treatments and/or the HIP treatment. Each casting process and heat treatment combination has certain advantages and disadvantages. From a material point of view, each casting process-post casting treatment combination results in a different microstructure, which can be characterised by the following microstructural features:

- casting defect, notably micro-shrinkage pores and gas porosity;
- the aluminium matrix, often characterised by the DAS (dendrite arm spacing), the SDAS (secondary dendrite arm spacing) and

- the precipitation hardening level;
- inclusions, in particular silicon particles in the eutectic zones and intermetallics.

The influence of these factors on the HCF behaviour of these materials has been investigated by many researchers. The effect of casting porosity has been studied by [1–4] and the effect of the microstructure (i.e. the aluminium matrix and the silicon particles) by [5–7]. However, these studies are often limited to uniaxial fatigue behaviour.

The principal aim of this work is to investigate the influence of different microstructural heterogeneities found in cast aluminium–silicon alloys on the HCF behaviour for different loading modes. Specifically, the fatigue damage mechanisms associated with the microstructural features discussed above are investigated. In order to achieve this aim, an extensive multiaxial HCF testing campaign was conducted, including uniaxial tension–compression loads, pure torsion and combined tension–torsion, on three different Al–Si alloys. These alloys were fabricated by three different processes and therefore they have significantly different microstructures, particularly in terms of their casting defect populations.

2. Cast aluminium alloys under investigation

Fig. 1 shows typical microstructural images of the aluminium alloys under investigation which highlight the different microstructural heterogeneities discussed above.

2.1. Manufacturing processes for the three investigated alloys

The three cast aluminium alloys investigated in this study, referred as alloys A, B and C, were elaborated by either gravity die casting or lost foam casting and then were subjected to either a standard T7 heat treatment or a Hot Isostatique Pressing (HIP) followed by a T7 treatment (see Table 1).

Alloy A corresponds to the gravity die cast material introduced in the work of Koutiri et al. [1]. This material is cast by PSA Peugeot–Citroen in the form of cylinder heads using their industrial production process, however certain modification was made in order to have a much larger volume of material from which fatigue specimens could be extracted. This was done be reducing the length of the inlet and exhaust cores (Fig. 2a). The resulting modified cylinder heads have blocked inlet and exhaust passages on the engine block mating surface (Fig. 2b). This resulted in layer of material with a maximum thickness of 10 mm from which the specimens (Fig. 7) can be extracted.

Lost foam casting is used to fabricate alloys B and C and the material is cast in the form of plates, 200 mm × 150 mm × 18 mm in size. This leads to a material with a high porosity volume fraction. Consequently, it should be noted that the microstructure and the defect size distribution of alloys B and C are not representative of the material present in industrially cast cylinder heads.

The two post-casting heat treatments are presented below:

- *HIP treatment*: tempering at a temperature of approximately 500 °C under a pressure of approximately 1000 bars.
- *T7 heat treatment*:
  ○ Solution heat-treatment for 5 h at a temperature of 535–540 °C.
  ○ Water quenching at a temperature of 60–70 °C.
  ○ Tempering at 200 °C for 5–5.5 h.
  ○ Cooling in ambient air.

Table 1 lists the chemical compositions, casting processes and heat treatments for each of the investigated materials.

2.2. Microstructure characterisation and monotonic mechanical properties

2.2.1. The aluminium matrix

The primary alpha matrix is typically characterised by the Secondary Dendrite Arm Spacing (SDAS). This quantity is determined by identifying individual aluminium dendrites, the SDAS is then measured as the distance between the secondary dendrite arms (Fig. 3(a)). Forty dendrites of each material were measured and the SDAS distributions of the three materials are shown in Fig. 3(b). It can be seen that the SDAS of alloy A ($SDAS_A = 42.3 \pm 9.7$ µm) is the smallest while that of material B ($SDAS_B = 77.3 \pm 18.9$ µm) and C ($SDAS_C = 91.4 \pm 32.8$ µm) are larger. For the casting of aluminium alloys the SDAS is inversely proportional to solidification rate [5]. As such the difference in the SDAS between alloys A and B/C can be explained by the fact that the solidification rate in gravity die casting in which metallic moulds are used (for alloy A) is greater than that in lost foam sand casting (alloys B and C).

As regard to the dendrite size, EBSD measurements have been conducted to characterise the distribution of the dendrite size. Three samples of alloys A and C with the same geometry as the fatigue specimens (Fig. 7(a)), but with a flat zone on the cylindrical section (see Fig. 7(b)), were prepared. The surface was firstly mechanically polished and then electrochemically etched using a 20:80 (%volume) HNO3/CH4Co solution at 0–5 °C and 15 V for 10 s. The spatial resolution of EBSD measurements is 5 µm × 5 µm. Fig. 4 shows an EBSD inverse pole figure cartography.

Using the data obtained by EBSD measurements, the grain size distributions are determined (Fig. 5). Note that these distributions are not based on the percentage of the number of grains but on the grain area percentage. The average grain size $D_{e,average}$ is then determined by the following equation [8]:

$$D_{e,average} = \Sigma_i(D_{e_i} \cdot f_i) \tag{1}$$

where $D_{e,i}$ is the equivalent diameter of grain i calculated from the area of grain i, $area_i$, by Eq. (2), and f_i is the grain size percentage of grain i

$$D_{e,i} = \sqrt{\frac{4 \times area_i}{\pi}} \tag{2}$$

The average grain size of alloy A (337 µm) is smaller than that of alloy C (464 µm). This difference is in agreement with the results obtained for the SDAS of these two alloys (Fig. 3(b)).

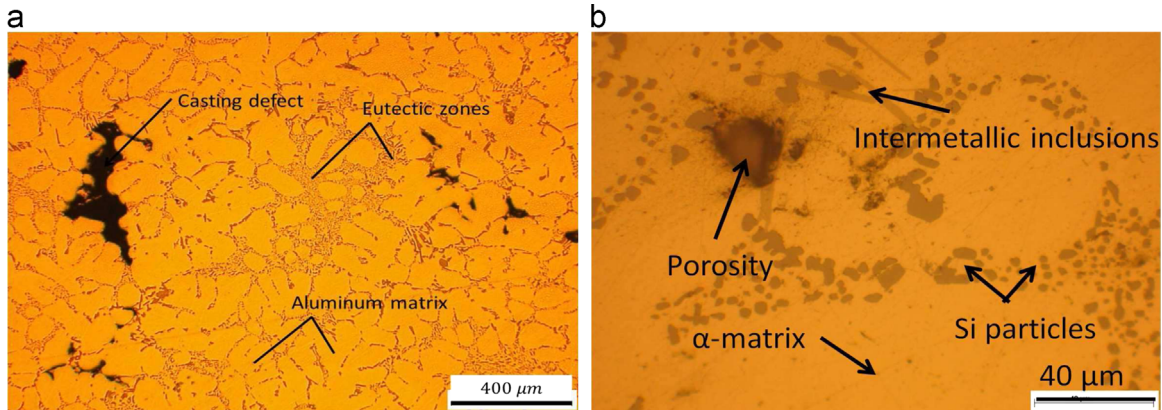In addition, the micro-hardnesses of the alpha phase of the

Fig. 1. Microstructural heterogeneities present in the cast aluminium alloys under investigation: (a) typical microstructure of cast aluminium alloys; (b) zoomed view.
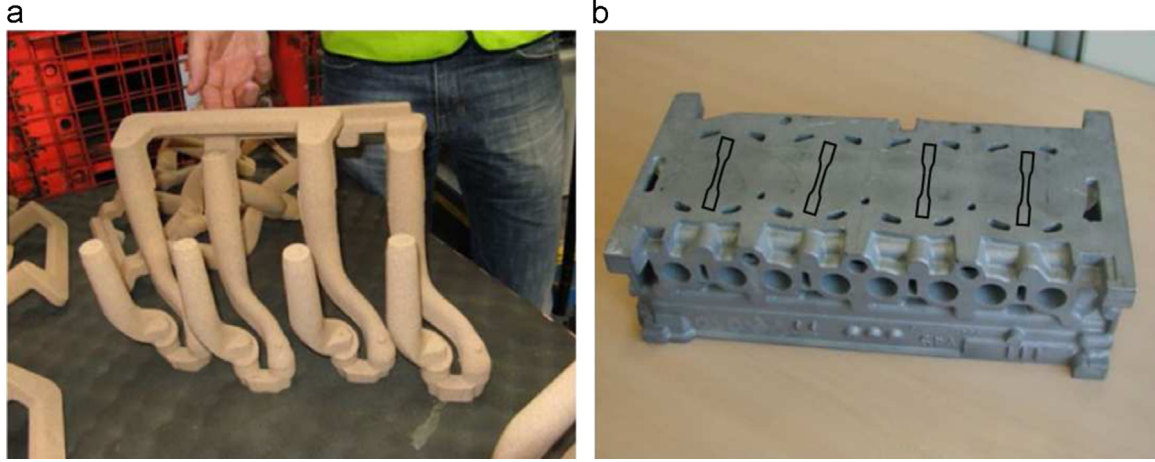
Fig. 2. (a) Modified cores used to shape the inlet and exhaust passages. (b) Cylinder head after modification [1].

- *The metallography methodology*: the defect size distribution is determined from optical microscopic observations of polished samples. In particular, the maximum defect size in each standard inspection area of size, S_0, is measured.
- *Observations of the failure surfaces*: the failure surface of each specimen, tested in fatigue, was examined to identify and measure the size of the casting defect at the origin of the fatigue failure for alloys A and B. No casting pore was found in the initiation zones for alloy C.

The defect size distributions determined for the three alloys, determined by the metallography methodology, are shown in Fig. 6(a) and the distributions based on observations of the failure surfaces for alloys A and B are shown in Fig. 6(b).

It shows that the defect sizes measured by the second method are much larger than those obtained by the first method. In fact, the distribution obtained by the first method corresponds to the extreme value distribution related to the area S_0 while the distribution determined by the second method is based on the assumption that the pore at the origin of the fatigue failure is the largest pore in the uniformly loaded volume. As such it corresponds to the extreme value distribution related to the critical defects in the total loaded volume. Because the sizes of these two observation zones are very different, the maximum defect sizes observed are different.

Because the obtained distributions correspond to the extreme

three alloys were measured (see Table 2). It can be seen that the micro-hardness of the alloy A is the highest while alloys B and C are approximately the same order of magnitude. In fact, alloy A contains an additional 0.5 wt% copper, compared to the alloys B and C. The presence of copper in the chemical composition results in a higher micro-hardness of the alpha phase.

2.2.2. Pore characterisation

In order to characterise the size distribution of the casting defect (degassing and micro-shrinkage pores) in these materials, two different methods are used: the metallography methodology proposed by Murakami [9] and a second approach based on observations of the fatigue failure surfaces:
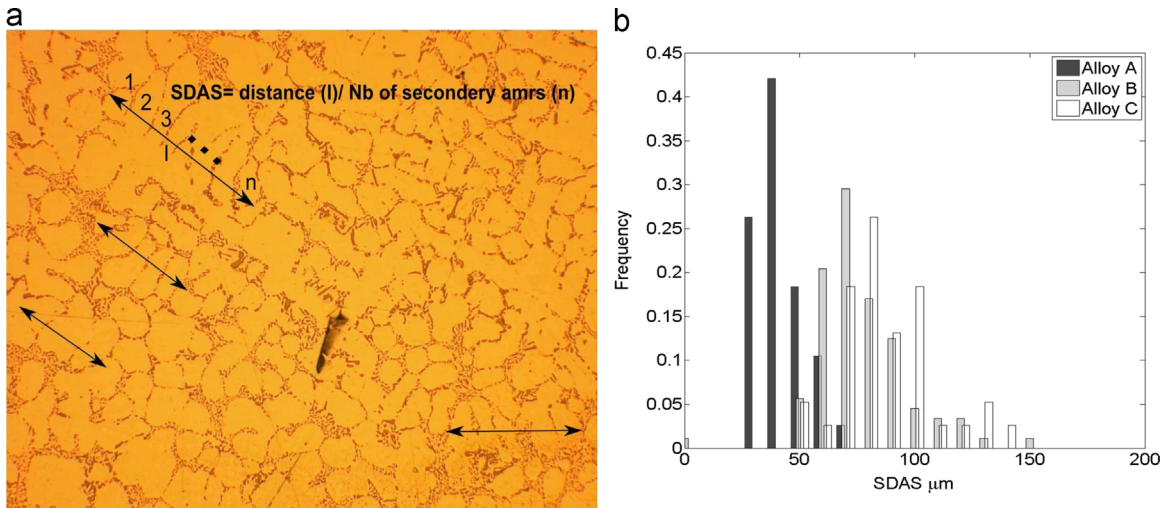

Fig. 3. SDAS measurement method (a) and the SDAS distributions of three materials under investigation (b).
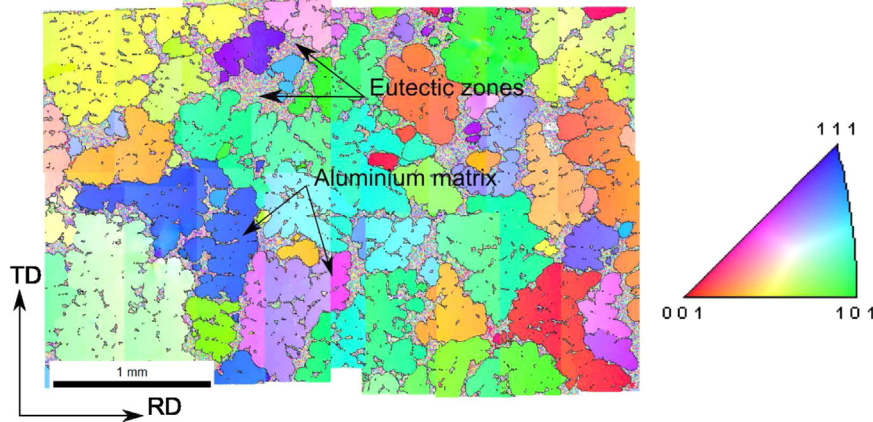
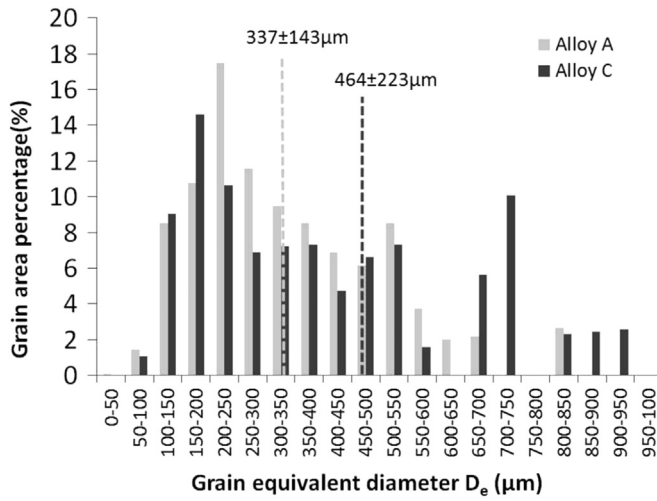**Fig. 4.** Inverse pole figure corresponding to the ND direction of the C sample.

Fig. 5. Grain size considering the grain size percentage distributions of alloys A and C.

Table 2
Micro-hardness of the aluminium matrix of the three investigated alloys.

Alloy	Micro-hardness ($\mu \pm s$) (HV0.025)
A	114 ± 3
B	99 ± 9
C	92 ± 13

value distribution, the Gumbel distribution has been used to fit the experimental data. It can be seen that the Gumbel distribution results in a very good approximation for alloys A and B for both methods.

2.2.3. Monotonic mechanical properties

The resulting mechanical properties of three alloys are listed in Table 3.

It is shown that all the mechanical properties (the Young modulus, yield stress, ultimate tensile strength and elongation) of alloy A are higher than that of alloy C, even though alloy A contains porosity and alloy C is porosity-free. However, it must be kept in mind that the alloy A has not only a finer microstructure than the alloy C ($SDAS_A < SDAS_C$) but also a higher micro-hardness of the alpha phase. These factors can significantly improve the mechanical properties of cast Al–Si alloys [10–12].

2.3. Experimental conditions: fatigue tests

All of the fatigue tests presented below were carried out at ambient temperature and pressure in laboratory air. All of the fatigue tests were conducted with the same specimen geometry, shown in Fig. 7(a). All of the fatigue specimens were mechanically polished after machining using (a) abrasive paper (b) followed by polishing using a diamond paste down to 1 µm in size and (c) finally an active oxide polishing suspension was used.

Table 4 summarises the fatigue testing conditions of the three loading conditions investigated. In order to determine the fatigue strength, the staircase technique was used with a maximum life of 2×10^6 cycles. The stopping criteria were chosen to ensure the presence of a fatigue crack of approximately 3 mm in length.

3. Fatigue strength for different loading conditions

Fig. 8(a), (b) and (c) shows the experimentally determined Wöhler diagrams for alloys A, B and C, for different loading modes. Note that for the combined tension–torsion loading condition the stress amplitude shown on the diagram corresponds to the axial stress $\sigma_{xx,a}$ ($\sigma_{xx,a} = 2\tau_{xy,a}$). The curves passing through the experimental data correspond to the Basquin equation $\sigma_{xx,a} = a. N^m$. The fatigue strengths at 2×10^6 cycles are presented in τ–σ space (or on the Gough–Pollard) diagram in Fig. 9. The error bars correspond to a failure probability of 10–90%, calculated from the standard deviations obtained thank to the stair-case technique.

Table 5 summarises the fatigue strengths, in terms of the mean value μ and standard deviation s of the three investigated alloys at 2×10^6 cycles.

Firstly, it can be seen that for the tension–compression and combined tension–torsion loading conditions, the fatigue strength of alloy C is the greatest and that of alloy B is the smallest. This tendency is in agreement with the casting defect populations determined for the three alloys (see Fig. 6(a)). For the purely torsional loads, a surprising result is observed: the fatigue strengths of alloys B and C are of the same order of magnitude, while alloy A has the highest fatigue strength.

A very interesting result is the change in the ratio between the torsional fatigue strength and the uniaxial fatigue strength ($\tau_{a,D}/\sigma_{a,D}$): for the porosity-containing alloys (alloys A and B), $\tau_{a,D}/\sigma_{a,D} \approx 1$ while for the porosity-free alloy (alloy C), $\tau_{a,D}/\sigma_{a,D} = 0.57$.

Another important point to consider is the scatter associated with the fatigue strength. The relative standard deviation (RSD), determined by Eq. (3), is used to estimate the scatter
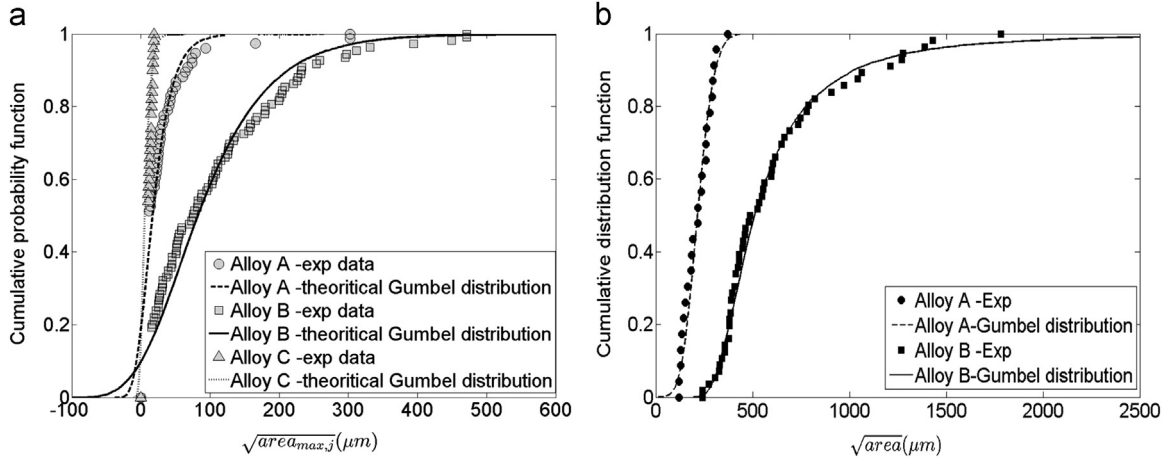
Fig. 6. Defect size distributions characterised by the two different methodologies: (a) by the metallography methodology; (b) by the observations of the failure surfaces.

Table 3
Mechanical properties of the three alloys.

Alloy	Young's modulus E ($\mu \pm s$) (GPa)	0.2% Yield stress σ_y ($\mu \pm s$) (MPa)	Ultimate tensile strength σ_{uts} ($\mu \pm s$) (MPa)	Elongation ($\mu \pm s$) (%)
A	77 ± 6	260 ± 2	304 ± 4	4.7 ± 1.2
B	68 ± 5	240 ± 5	251 ± 6	0.8 ± 1.2
C	74 ± 3	250 ± 3	275 ± 5	2.3 ± 0.7

$$RSD = \frac{s}{\mu} \tag{3}$$

where μ and s are the mean value and the standard deviation of the experimentally determined fatigue strength, respectively. For the combined tension–torsion load, the axial fatigue amplitude ($\sigma_{xx,a,D}$) is used in this calculation.

Fig. 10 shows the relative standard deviation of the three investigated alloys for different loading modes. It is shown that the RSD of the porosity-free alloy (alloy C) for the tension–compression and combined tension–torsion loading conditions is lower than that of the porosity-containing alloys (alloys A and B).

Table 4
Fatigue test conditions for different loading modes.

Load	Load ratio, R	Biaxiality ratio, K	Machine	Frequency (Hz)
Pure tension	-1	N/A	Resonant	90–100
Pure torsion	-1	N/A	Resonant	70–90
Combined tension–torsion	-1	0.5	Electromagnetic	20–30

4. Fatigue crack initiation and crack growth mechanisms under different loading modes

4.1. Uniaxial loading

4.1.1. Porosity-containing materials (alloys A and B)

Surface observations (using an optical microscope) and observations of the failure surfaces (using a scanning electron microscope, SEM)) show that, for uniaxial loads (plane bending and tension–compression loading $R = -1$), the fatigue cracks always initiate from pores (see Fig. 11) in alloys A and B. These observations are in good agreement with experimental observations reported in the literature [1,4,8,13–21,3]
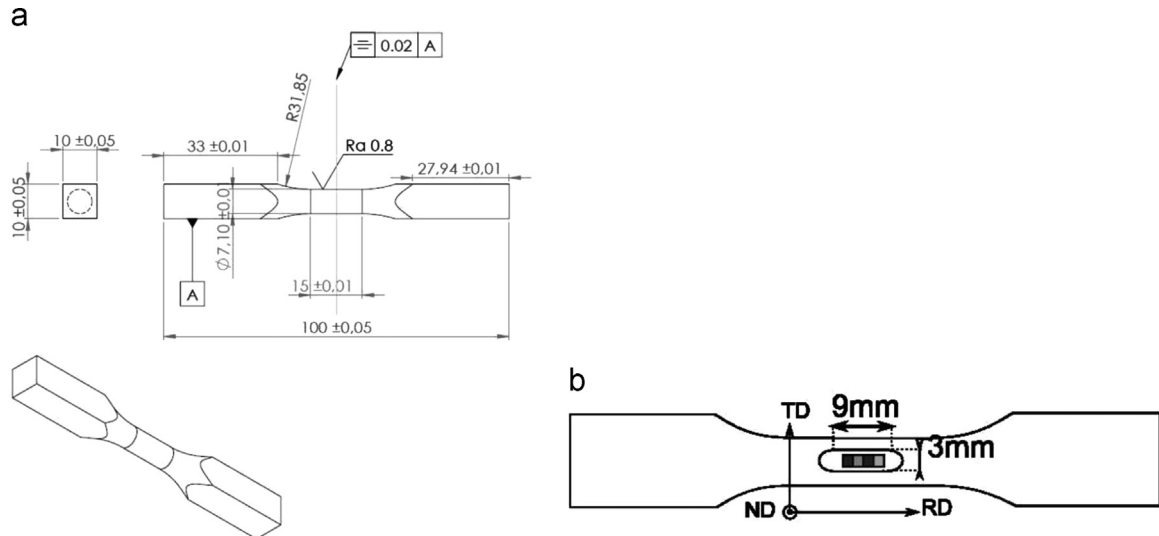

Fig. 7. Specimen for tension, torsion and combined tension–torsion fatigue tests (a) and dimensions of flat zone polished on the fatigue specimen used for EBSD observations (b).
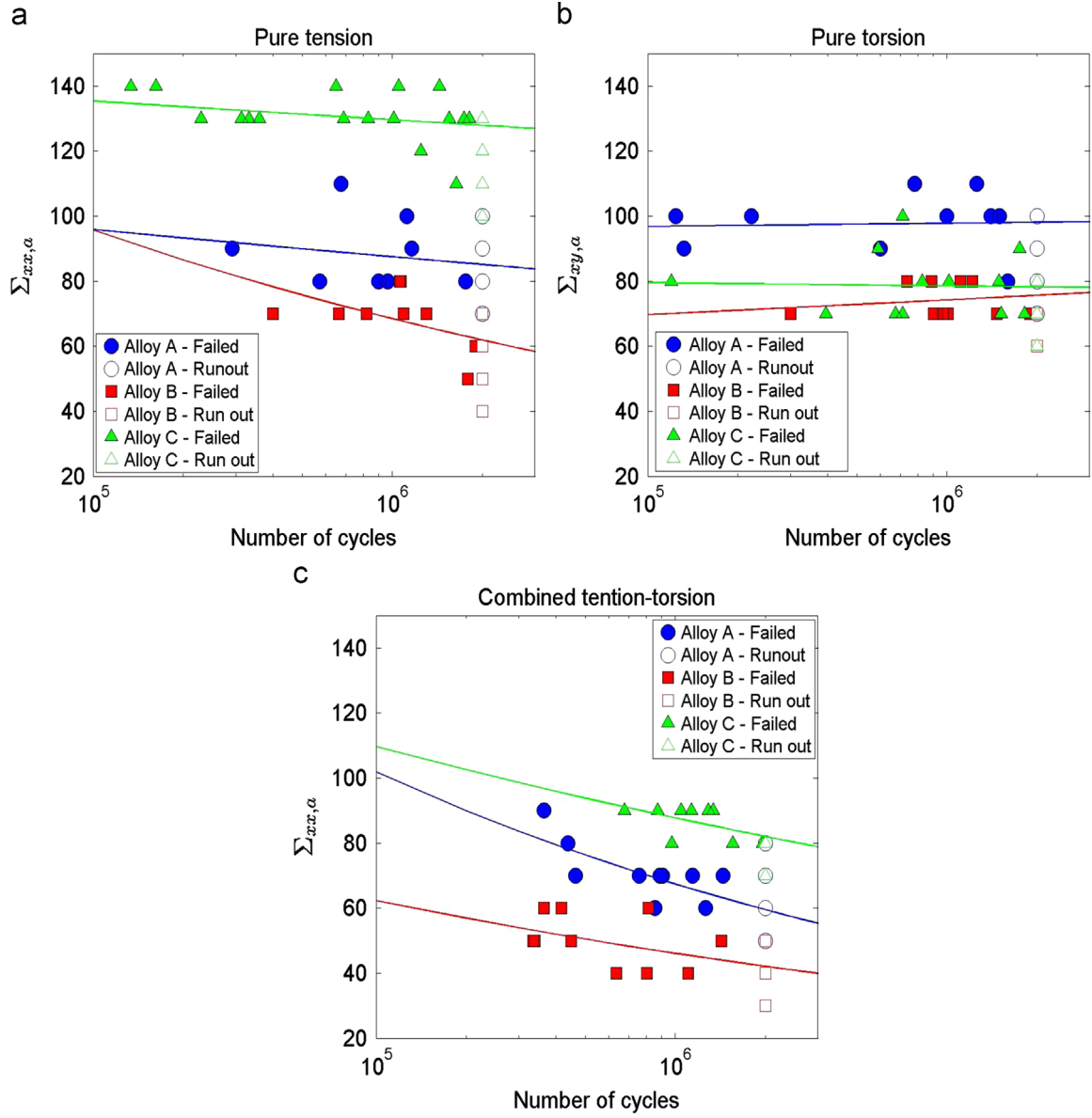
Fig. 8. Wöhler diagrams for alloys A, B and C for (a) uniaxial tensile loads $R = -1$; (b) reversed torsion load $R = -1$(b); (c) combined tension–torsion load $R = -1$.
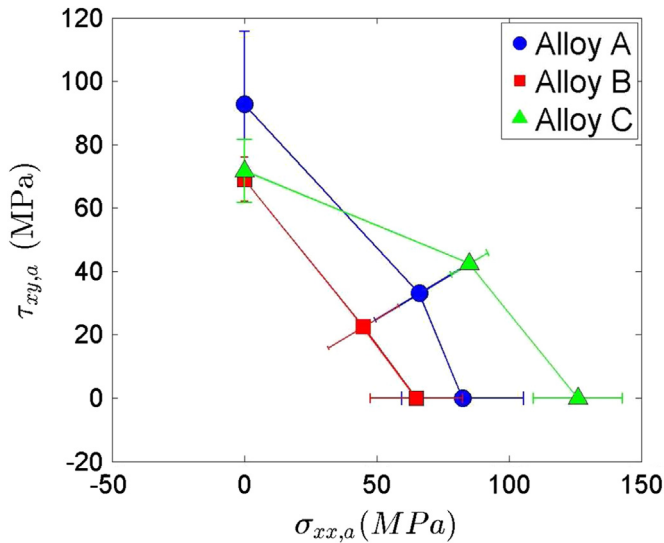

Fig. 9. $\tau_{xy,a} - \sigma_{xx,a}$ diagram of three studied alloys.

Table 5
Summary of the fatigue strengths of the three alloys at 2×10^6 cycles for different multiaxial loading loads.

| Alloy | Pure tension (alloys B and C) | Pure torsion | Combined tension-torsion |
	Plane bending (alloy A) $(\mu \pm s)$ (MPa)	$(\mu \pm s)$ (MPa)	$\sigma_{xx,a}(= 2\tau_{xy,a})(\mu \pm s)$(MPa)
A	83 ± 18	93 ± 14	66 ± 13
B	65 ± 13	69 ± 5	49 ± 10
C	126 ± 13	72 ± 8	80 ± 5

4.1.2. Porosity-free material (alloy C)

Two fatigue crack initiation mechanisms have been observed to operate in alloy C: the first mechanism is associated with persistent slip bands (PSB) formation and the second is controlled by oxide films. In the literature, these two crack initiation mechanisms have also been reported in the work of Wang et al. [5] and Zeng et al. [22].
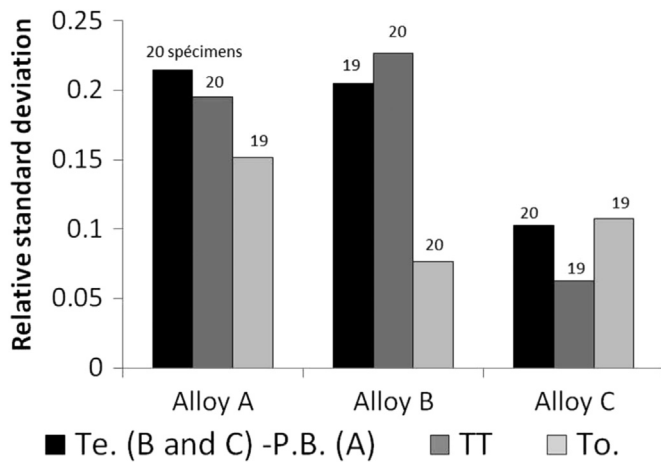
Fig. 10. Comparison of relative standard deviation associated with the fatigue strength of alloys A, B and C for different loading modes: pure tension (Te.), plane bending (P.B.), combined tension–torsion (TT) and pure torsion (To.)

Crack initiation from PSB: this mechanism was observed in 14 of 20 specimens. Fig. 12 shows a fatigue crack which initiates from a PSB. The size of the crack initiation site is approximately 400 μm. This value is in good agreement with the mean value of the grain size of alloy C (see Fig. 5).

Crack initiation by oxide film: this mechanism was observed in 6 of 20 specimens. In order to identify this initiation mechanism, energy-dispersive X-ray spectroscopy (EDS) analyses were used to determine the chemical compositions at the crack initiation sites. Fig. 13 shows that oxygen and aluminium are the most abundant elements.

In the work of Koutiri et al. [1], the authors observed another crack initiation mechanism related to damage associated with silicon particles in eutectic zones (i.e. rupture or debonding of the silicon particles). However, it should be kept in mind that alloy A contains casting pores and that the authors observed that the "dominating" damage mechanism was related to the porosity. Following the observations of the crack initiation mechanisms in alloys B and C for uniaxial loading $R = -1$ in which damaged silicon particles were not observed, it is proposed here that crack initiation in the eutectic zones of alloy A is probably caused by pores located just below the surface.

4.2. Pure torsion loading

4.2.1. Porosity-containing materials (alloys A and B)

In the work of Koutiri et al. [1,23], observations of the specimen surfaces as well as the fatigue failure surfaces of alloy A showed that crack initiation is not related to the porosity for pure torsional loads. According to the authors, when loaded in torsion, casting pores have much less influence when compared to the uniaxial loading condition. Concerning the principal fatigue cracks, for the majority of cases, cracks were observed to initiate in the plane of maximum shear stress, perpendicular to or parallel to the specimen axis. No crack bifurcation was observed during propagation.

For alloy B, two crack initiation mechanisms were observed: the first mechanism is related to crack propagation from pores located on the specimen surface and the second is controlled by PSB formation (see Fig. 14). These two mechanisms coexist and have been observed on the same specimen.

Regarding the crack propagation mechanisms, a competition between two propagation mechanisms can be observed: the first one is related to the opening mode (mode I) and the second is controlled by the shear stress (modes II and III). Fig. 15 shows the crack size and shape corresponding to different numbers of cycles of a fatigue crack observed on a specimen subjected to pure
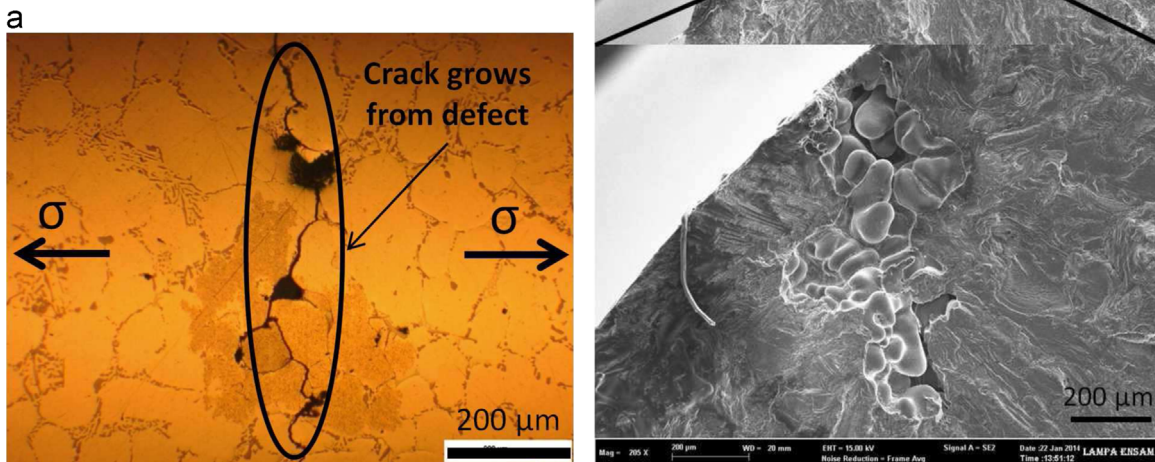

Fig. 11. Fatigue crack initiation from a degassing pore in alloy B for the tension–compression load with an $R = -1$: (a) surface observation; (b) observation of the failure surface.
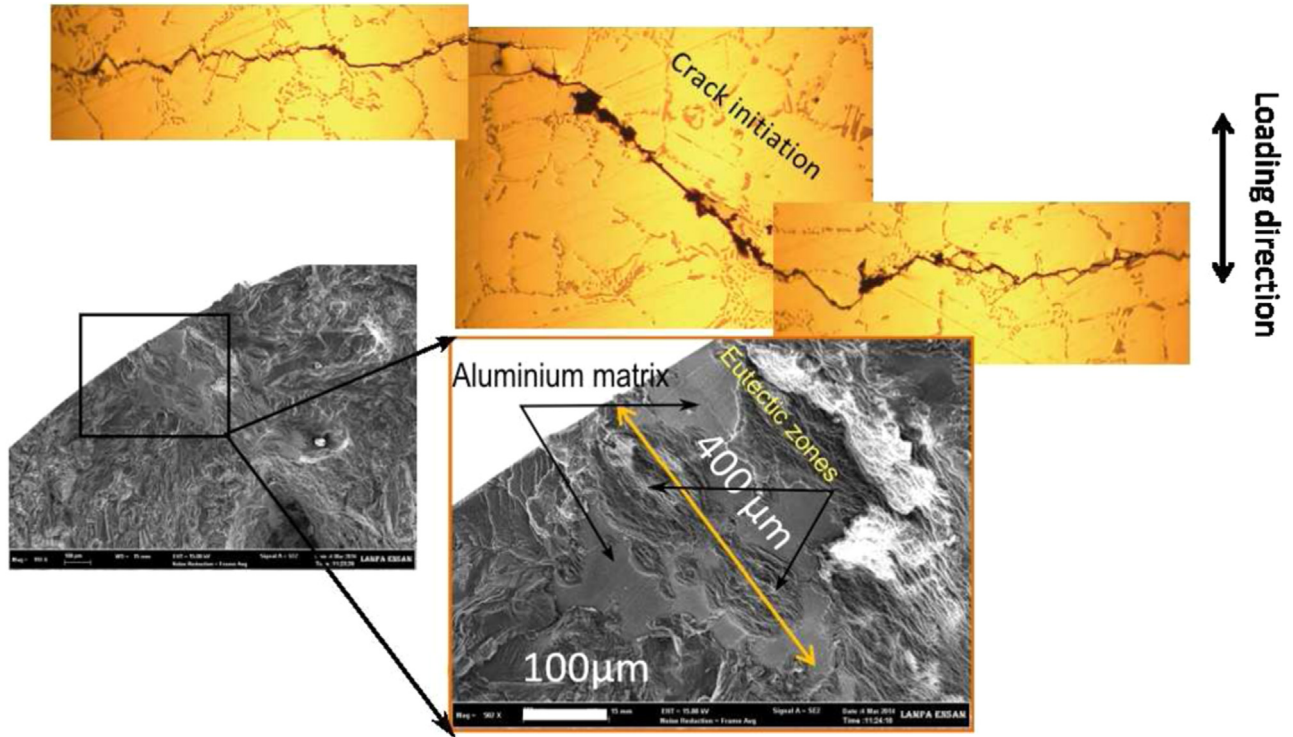
Fig. 12. Crack initiation from PSB, observed on the specimen surface and on the failure surface of alloy C. The specimen is loaded in pure tension $\sigma_{xx,a} = 120$ MPa, $N_f = 1.4 \times 10^6$ cycles

torsion with $\tau_{xy} = 80$ MPa ($R = -1$).

4.2.2. Porosity-free material (alloy C)

For alloy C, it is observed that crack initiations are always controlled by PSB formation (see Fig. 16).

It has also been observed that many cracks related to PSB were blocked by grain boundaries (or dendrite boundaries) when the crystallographic orientations of the blocking grains are not favourable in terms of the crack growth direction (see Fig. 17)

Concerning crack growth, for the majority of cases, fatigue cracks propagate due to a shear mode for pure torsion loads. However, it is possible to observe crack bifurcation controlled by either a shear mode or by the opening mode.

4.3. Combined tension–torsion loading with $k = \tau_a/\sigma_a = 0.5$

The fatigue damage mechanisms in combined tension–torsion with a biaxiality ratio $k = \tau_a/\sigma_a = 0.5$ are similar to those observed for the pure tension–compression load case. That is:

- for the porosity-containing alloys (alloys A and B), fatigue cracks initiate from pore and grow in the plane of maximum normal stress;
- for the porosity-free alloy (alloy C), fatigue cracks initiate from PSB and grow in the plane of maximum normal stress.

4.4. Summary of fatigue damage mechanisms

Fig. 18 summarises the crack initiation mechanisms observed on the surface of the three alloys for different loading modes.
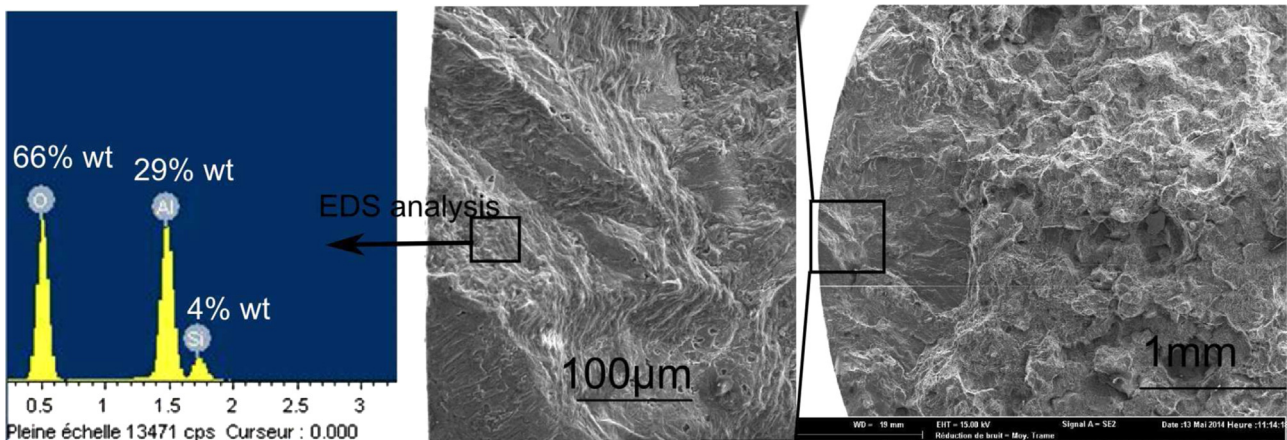

Fig. 13. Crack initiation due to the presence of an oxide film in pure tension loads. The local chemical composition and SEM observations of the failure surface for a specimen of alloy C.
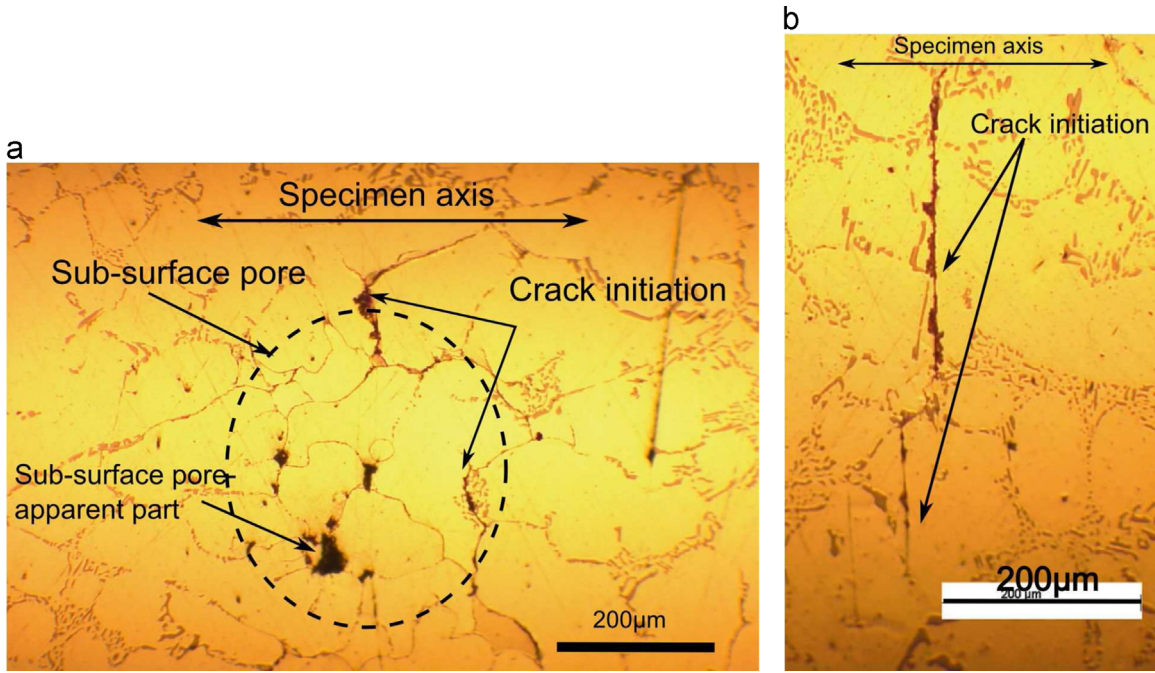
Fig. 14. Two crack initiation mechanisms observed for the pure torsion loads of alloy B: (a) crack initiation at a pore; (b) crack initiation by PSB.
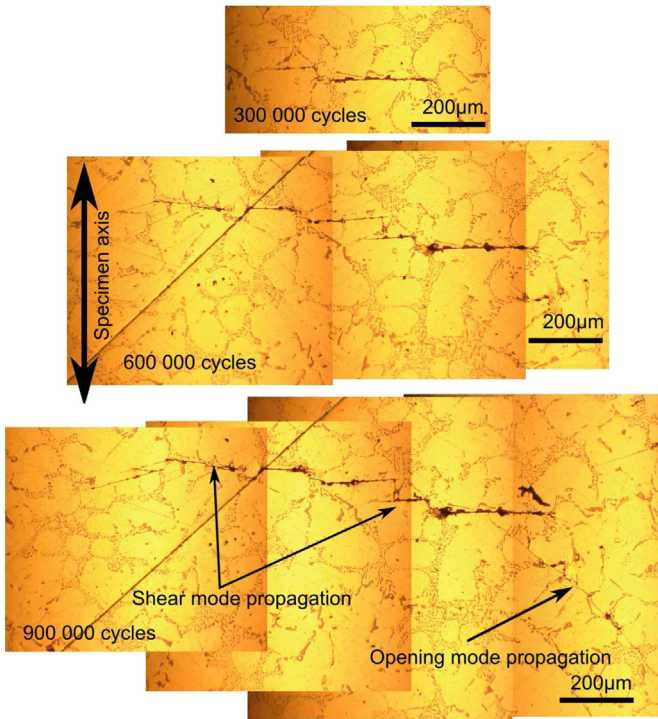

Fig. 15. Crack growth observation for an alloy B specimen subjected to pure torsion with $\tau_a = 80$ MPa, $N_f = 1.9 \times 10^6$ cycles.

- *For pure tension and combined tension–torsion loads*: fatigue cracks always initiate and propagate from pores for the porosity-containing materials (alloys A and B) while for the porosity-free alloy (alloy C), fatigue cracks initiate from persistent slip bands (PSB).
- *For pure torsional load*: for the porosity-containing alloys (alloys A and B), two crack initiation mechanisms have been observed: the first mechanism is related to crack propagation from casting pores located on the specimen surface and the second is controlled by PSB formation. These two mechanisms coexist and
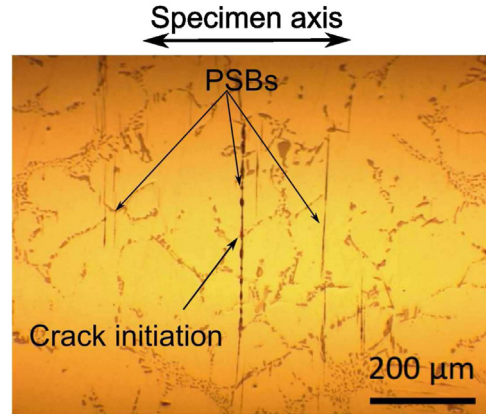

Fig. 16. Crack initiation from PSB observed on the specimen surface of alloy C subjected to pure torsion with $\tau_a = 70$ MPa at $N = 2 \cdot 10^6$ cycles.

have been observed on the same specimen. For the porosity-free alloy (alloy C), only the crack initiation mechanism related to PSB formation was observed.

Based on these fatigue damages mechanism observations, the change in the ratio between the torsional fatigue strength and the uniaxial fatigue strength ($\tau_{a,D}/\sigma_{a,D}$) mentioned in Section 3 can be explained by the fact that casting pores have lower influence when loaded in pure torsion, compared to the other loading conditions (tension–compression and combined tension–torsion) for the porosity-alloys (alloys A and B).

The difference in the relative standard deviation of the fatigue strengths (see Section 3) can be explained by the fact that the fatigue damage mechanism for alloy C is related to PSB formation regardless of loading modes while for alloys A and B, the fatigue damage mechanism is controlled by crack propagation from pores, particularly for uniaxial loads and combined tension–torsion load. This explanation is confirmed by the lower scatter associated with the fatigue strength for the pure torsion load, compared to the tension–compression and combined tension–torsion loads, for
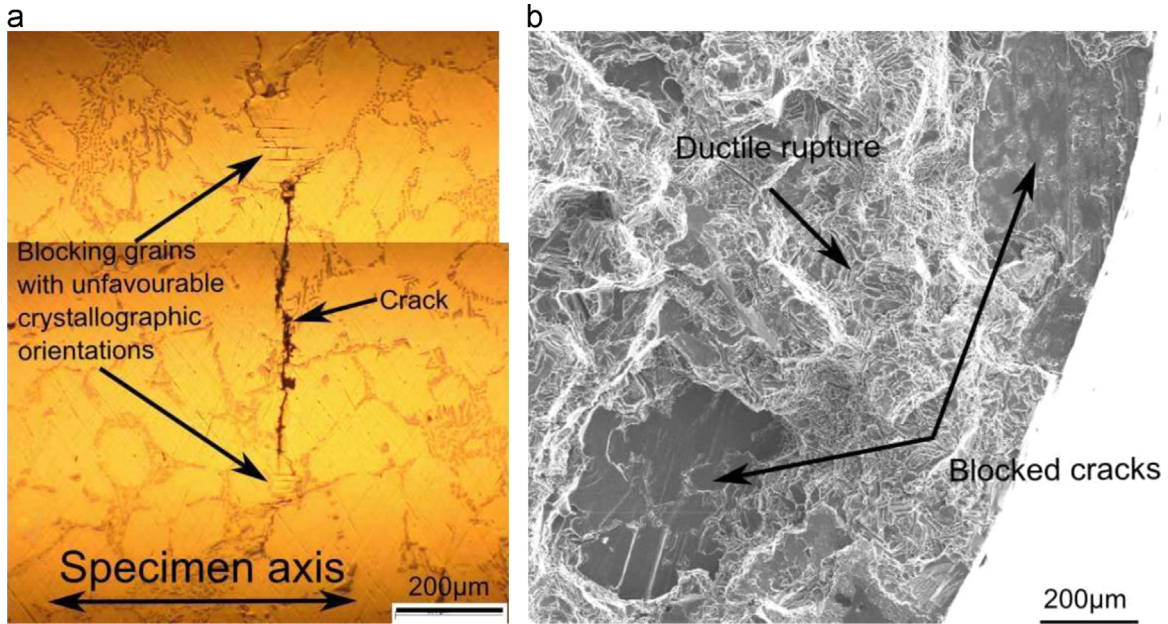
Fig. 17. Blocked cracks due to the grains with unfavourable crystallographic orientation observed on a specimen surface (a) and on a failure surface (b) for the pure torsional load of the alloy C.

alloys A and B.

5. Roles of aluminium matrix and silicon particles in PSB formation in pure torsion load

As discussed earlier, for the porosity-free alloy (alloy C), fatigue cracks initiate systematically from PSB, regardless of the loading mode. In this section, the mechanism resulting in PSB formation for pure torsion will be investigated to determine the respective roles of silicon particles in the eutectic zones and the aluminium matrix.

5.1. The role of the aluminium matrix

In order to estimate the role of the aluminium matrix in the formation of the PSB, EBSD measurements were undertaken on three specimens with the geometry shown in Fig. 7. These specimens were subjected to a pure torsional load ($R = -1$) until the presence of PSB was observed (see Fig. 19). Table 6 summaries the test conditions.

In order to analyse the influence of the crystallographic orientations on PSB formation, the effective Schmid factor (ESF), introduced by Agbessi et al. and Robert et al. [24,25], is used. This factor is defined by the following equations:
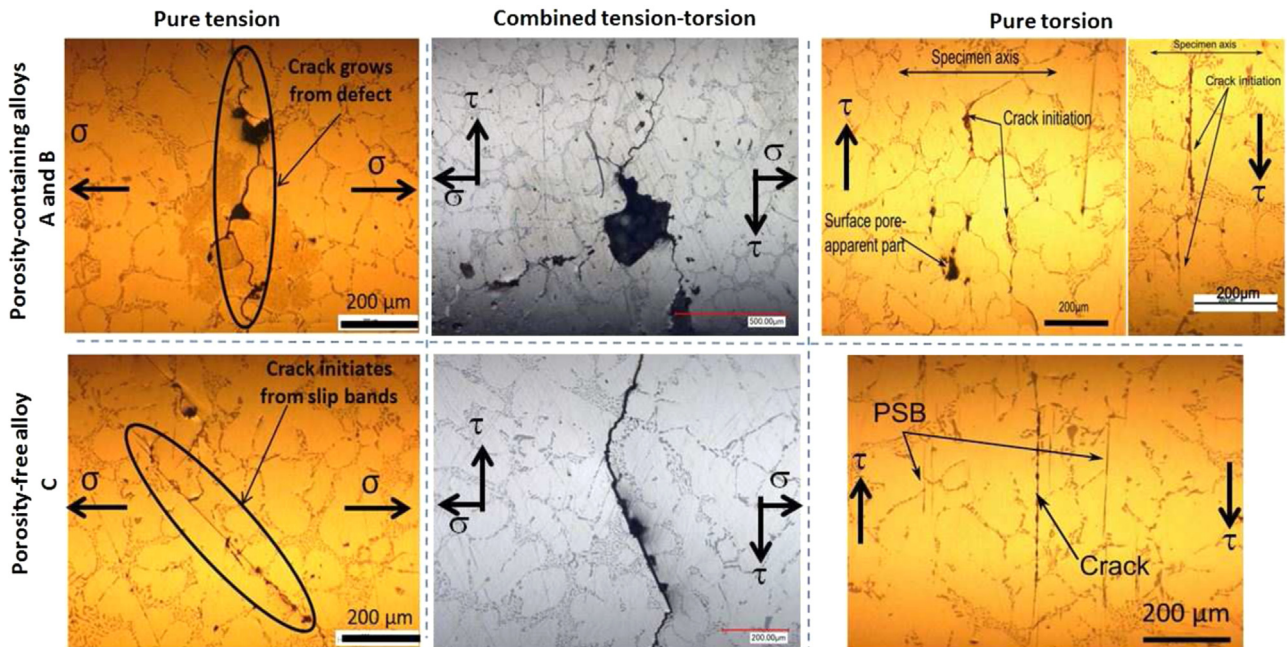

Fig. 18. Fatigue damage mechanisms of alloys A, B and C for three loading modes (pure tension, combined tension-torsion and pure torsion), observed on the specimen surfaces.
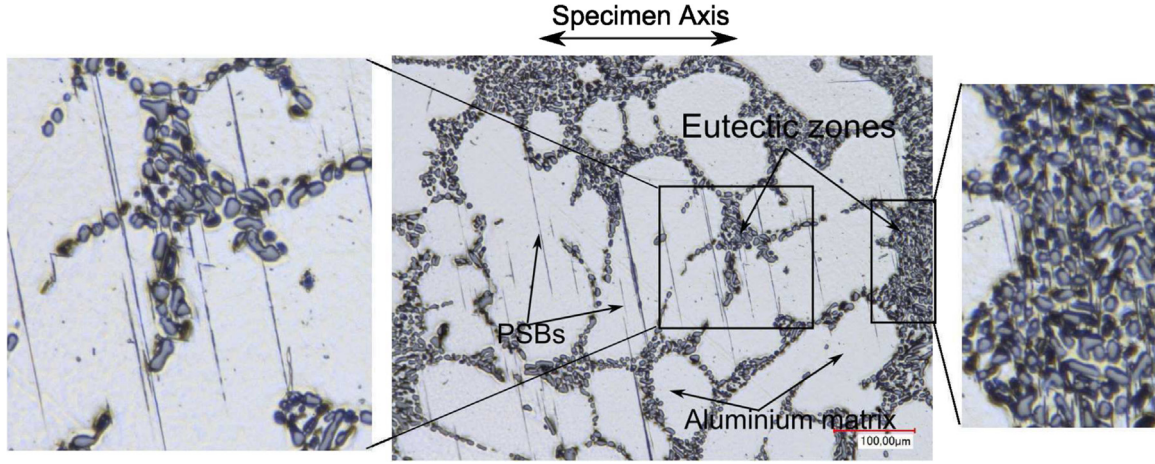
Fig. 19. PSB observed on an alloy C specimen subject to pure torsion with $\tau_a = 80$ MPa at N = 2.2×10^6 cycles.

Table 6
Resume of pure torsion loading test for EBSD observations.

Alloy	Specimen	τ_{max} (MPa) in the observation zone	Number of cycles
A	1	90	2.5×10^6
C	2	80	2.2×10^6
C	3	90	1.3×10^6

$$f_{eff,g}^s = \max_t \left(\frac{\tau_g^s(t)}{\Sigma_l(t)} \right) \tag{4}$$

$$\tau_g^s(t) = \underline{m}^s . \underline{C}(t) \tag{5}$$

$$\underline{C}(t) = \underline{\Sigma}_n(t) - \underline{N}(t) = \underline{\Sigma}(t). \underline{n}^s - (\underline{n}^s. \underline{\Sigma}(t). \underline{n}^s)\underline{n}^s \tag{6}$$

where $\tau^s(t)$ is the resolved shear stress on slip system s defined by the normal vector $\underline{n}^s$ and the slip direction vector $\underline{m}^s$ of grain g. $\underline{\Sigma}(t)$, $\underline{\Sigma}_n(t)$ and $\Sigma_l(t)$ are the stress tensor, the normal stress vector and the largest component, respectively, of the principal stress tensor at the macroscopic scale, $\underline{\Sigma}_P(t)$. Using this definition of ESF, the maximum value of the ESF is 0.5 for uniaxial loads and 1.0 for pure torsional load. After obtaining the Euler angles of the grains using EBSD data, the ESF corresponding to each slip system of grains is determined. Because aluminium has a face-centred cubic (fcc) crystal structure, there are 12 slip systems constituted from 4 slip plans {111} and 3 directions <110>.

Firstly, the experimentally observed directions of the PSB were compared with the theoretical predictions for the slip systems of each grain. It was observed that the experimentally observed directions are *always* aligned with the theoretical directions of the slip planes in which the ESF is maximum of the four slips planes {111}. However, it is impossible to determine the direction (between the 3 directions <110>) in which the observed PSB were formed. Therefore, it is assumed that the experimentally observed PSB correspond to the slip system which maximises the ESF.

Furthermore, because the flat zone, machined on the specimen surface to facilitate the EBSD measurements, is relatively large compared to the cross section of the specimen, its presence leads to an high stress gradient in this zone. Therefore, it draws the relationship between the probability of occurrence of PSB against the maximum resolved shear stress instead of against the ESF. The maximum resolved shear stress is calculated by the following equation:

$$\tau_{eff,g}(t) = \max_{i=1..12} (f_{eff,g}^{s_i}). \Sigma_l(t) \tag{7}$$

where $f_{eff,g}^{s_i}$ is the ESF corresponding to slip system s_i of the grain g and $\Sigma_l(t)$ is the largest component of the principal stress tensor at macroscopic scale applied on grain g, $\underline{\Sigma}_P^g(t)$. This stress is determined from a 3D finite element simulation of the specimen in which an isotropic elastic material is used and the spatial position of the center of the grain g. It is assumed that there is no effect of grain boundary, grain crystallographic orientation and phase on the stress field.

Fig. 20 shows the probability of occurrence of PSB as a function of the resolved shear stress. The probability of occurrence of PSB corresponding to resolved shear stress, τ_i, is calculated as the ratio between the number of grains having the resolved shear stress τ_i in which PSB are observed and the total number of grains having the resolved shear stress τ_i. There are approximately 100 grains in total considered in each sample.

This figure shows that the occurrence probability of PSB depends on the resolved shear stress. The threshold of the resolved shear stress resulting in the apparition of the first PSB is highlighted. The comparison between the two alloy C specimens (specimens 2 and 3) shows that this threshold is not a constant but depends also on the number of cycles: at a lower resolved shear stress, the number of cycles necessary for the formation of the first PSB is higher. This relationship was also observed in the works of [24,26].
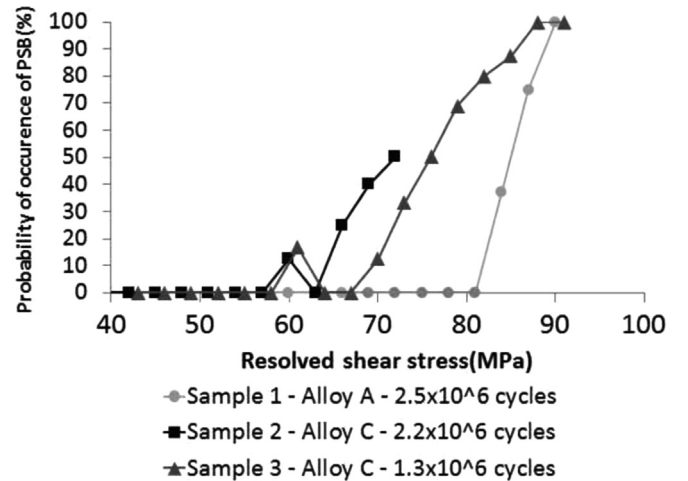

Fig. 20. Relationship between the probability of occurrence of PSB and the maximum resolved shear stress.

By comparing the sample 1 (alloy A) and sample 2 (alloy C) the influence of the aluminium matrix can be determined. These specimens were loaded until approximately the same number of cycles. However, an significant difference of the threshold of the resolved shear stress between these two alloys is observed. This difference can be explained by the following factors:

- *The precipitation hardening level*: alloy A (AlSi7Cu05Mg03-KT7) contains an additional 0.5 wt% copper compared to alloys B and C. Therefore the hardening precipitates of alloy A are mostly binary precipitates $\beta'(Mg_2Si)$ and quaternary precipitates $Q''/Q'(Al_5Cu_2Mg_8Si_7)$ [27]. For alloys B and C, the absence of copper is assumed to lead to a lower volume fraction of hardening precipitates of the alpha phase. This effect can be observed via the comparison of the micro-hardness of the alpha matrix between the three alloys: the micro-hardness of alloy A (113.8 ± 2.8 Hv0.025) is the highest while the one of alloys B (99 ± 9 Hv0.025) and alloy C (92 ± 13 Hv0.025) are relatively similar given the scatter.
- *The SDAS*: alloy A has a finer microstructure than alloy C ($SDAS_A < SDAS_C$). The SDAS could influence the threshold of the resolved shear stress via the grain boundary effect. However, this effect has not been investigated in the present work.

5.2. The role of silicon particles

It is seen in Fig. 19 that the majority of PSB initiate from silicon particles. This fact suggests that the silicon particles facilitate PSB formation. In order to investigate the competition of the roles of the aluminium matrix and the silicon particles in the formation of PSB, Fig. 21 shows a comparison of the maximum effective Schmid factors of the grains without PSB and the grains in which PSB are observed. Because the observations zone is small, the calculation of the resolved shear stress is not necessary .

It is shown that PSB initiation occurs only at silicon particles related to the grains having a high ESF (grains 1 and 4). No PSB were observed in grains 2 and 3.

Also, it can be seen in Fig. 19 that PSB also initiate at silicon particles in the eutectic zones. However the high density of silicon particles in these zones can confine the development of PSB in these areas.

5.3. Partial conclusion

Thank to analysis in Sections 5.1 and 5.2, the following conclusions can be made for pure torsion loads at $R = -1$:

- the role of the crystallographic orientations, the precipitation hardening level and the SDAS of the aluminum matrix are the major factors defining in which grain PSB formation occurs;
- the silicon particles play the role of initiating the PSB, only if the conditions above are satisfied and given that silicon particles can be found surrounding all grains, the role of the Si particles is not decisive in PSB formation.

It would not be unreasonable to assume that this conclusion is valid for uniaxial loads with $R = -1$ because crack initiation is principally controlled by PSB formations and no cracked or debonded Si particles were observed at the crack initiation sites for alloy C. However, for a loading condition with higher hydrostatic stress (for example uniaxial loads with positive load ratio), this conclusion may no longer be valid. For example, the work of Dezecot and Brochu [28] shows a more detrimental role of Si particles (cracked and/or debonded Si particles observed in crack initiation sites) in cast aluminum alloys for uniaxial loads at $R = 0.1$.

Thank to this analysis, the higher torsional fatigue strength of alloy A compared to alloy C (see Section 3) can be explained by the following factors:

- *A lower influence of the porosity on the torsional fatigue strength*: even though alloy A contains casting pores, the fatigue damage mechanism related to the formation of PSB dominates for the pure torsion load.
- *The precipitation hardening level of the alpha phase*: alloy A contains an additional 0.5 wt% copper compared to alloys B and C. This gives alloy A a higher critical shear stress compared to alloys B and C.

However, it should be kept in mind that it has been assumed that there is no effect of the grain boundaries (or the effect of grain size/SDAS) on the stress field when calculating the resolved shear stress.

In the literature, the effect of the SDAS on the fatigue strength of the porosity-free alloys has not been well investigated. The following exceptions can be noted:

- *For uniaxial loads*: Wang et al. [5], Gao et al. [20] and Redik et al. [6] observed that for a SDAS from 30 to 60 μm, when the SDAS is increased, the fatigue strength decreases for a load ratio of $R = -1$. In the interval of SDAS from 60 to 80 μm, when the SDAS is increased, the fatigue strength increases [5]. However, Houria et al. [29] observed that the influence of the SDAS on the fatigue strength for uniaxial loads at $R = -1$ is not significant.
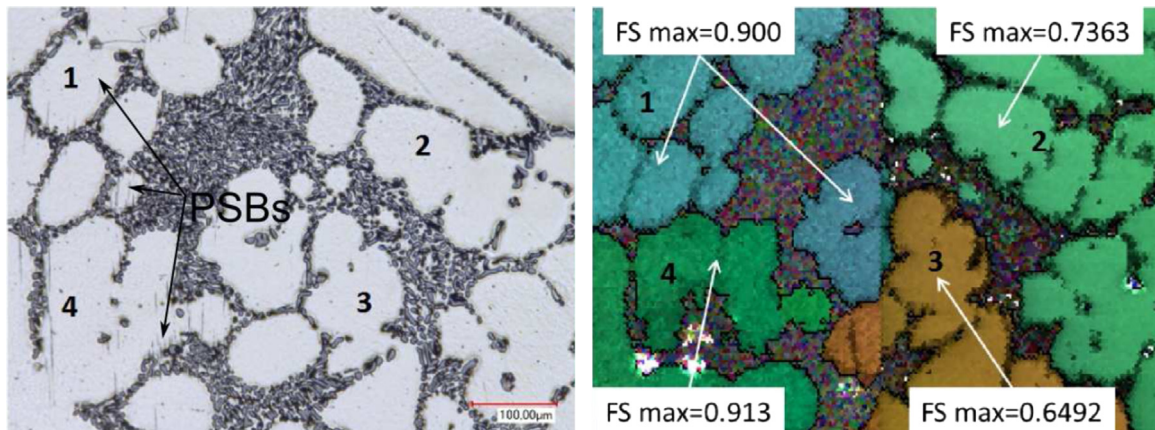- *For multiaxial loads*: only the work of Houria et al. [29] was

Fig. 21. Comparison of the ESF max of the grains with PSB and the grains without PSB.

found which investigated the effect of SDAS on the torsional fatigue strength. They observed that when the SDAS is increased, the torsional fatigue strength at a load ratio of $R = -1$ decreases.

The literature highlights the complicated role of the SDAS on the fatigue strength. Hence, more work is needed to completely understand the role of SDAS and its interaction with the precipitate hardening level in the alpha phase, for the formation of PSB.

6. Influence of the casting pores on the fatigue strength for different loading modes

6.1. Influence of defect for the tension–compression and combined tension–torsion loads

In order to investigate the influence of casting pores on the fatigue strengths, the failure surfaces were examined. The specimens that survived 2×10^6 cycles in the staircase procedure were retested at a stress amplitude one step higher, or 10 MPa higher for an additional 2×10^6 cycles. This was repeated until failure of the specimen after less than 2×10^6 cycles. The fatigue strength of the specimen was then taken to be the stress level of the final step. This method was firstly proposed by Maxwell et al. [30] and is regularly used by Nadot and co-workers for HCF tests of cast aluminium alloys [13,14,8].

The failure surfaces were examined and the pore at the origin of the principal crack was identified and measured using an scanning electro microscopy (SEM). Fig. 22 shows an example of defect area measurement.

Fig. 23 shows the experimentally determined fatigue strengths as a function of the experimentally determined defect size for alloys A and B for the tension–compression and combined tension–torsion loads. For each case, the experimental data are compared to the fatigue strength predictions using the LEFM criterion in which the fatigue strength is determined by the following expression [9]:

2. $\sigma_{I,a,D} = \dfrac{\Delta K_{th}}{0.65\sqrt{\pi\sqrt{area}}}$ (8)

where $\sigma_{I,a}$ is the amplitude of the principal stress and ΔK_{th} is the range of stress intensity factor (SIF) threshold in pure tension loading $R = -1$. These stress intensity thresholds have been arbitrarily estimated to match the experimental data.

In the literature, no data concerning the stress intensity threshold of artificial long cracks for uniaxial load $R = -1$ was found for cast Al–Si alloys. However, threshold data for a load ratio of $R = 0.1$ has been reported by [17,19,31], in which the threshold values for long cracks are estimated to be $\Delta K_{th} = 4\text{–}5\,\text{MPa}\sqrt{m}$.
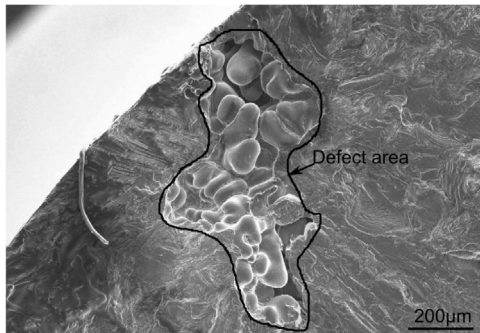

Fig. 22. Defect size measurement by observation of failure surface.

Compared to the stress intensity threshold estimated in Fig. 23 of approximately 2–3 MPa$\sqrt{m}$ at $R = -1$, it can be assumed that the small crack effect is significant for the propagation of natural fatigue cracks. In addition, it can be seen that the intersection of the fatigue strength of the porosity-free alloy (alloy C, the horizontal dotted line corresponding to 126 MPa) and the predictions using the LEFM criterion is approximately $\sqrt{area} = 100\text{–}200\,\mu m$. Consequently, it can be supposed that the critical defect size related to the uniaxial and combined tension–torsion loads is approximately $\sqrt{area} \approx 100\text{–}200\,\mu m$.

6.2. Influence of defect on pure torsion load fatigue strength

As mentioned earlier in Section 4, two fatigue damage mechanisms have been observed for the pure torsional loads in alloy B: the first one is related to crack propagation from casting defect in the opening mode; the second is controlled by the crack initiation from PSB followed by crack propagation in shear mode. Hence, the defects observed on the failure surfaces related to each mechanism were identified and measured. Fig. 24 shows the relationship between the defect size and the experimentally determined fatigue strengths corresponding to these two mechanisms. The defect size corresponds to the projected area $\sqrt{area}$ on the plane perpendicular to the specimen axis. It is important to note that for the second mechanism, because crack initiation and crack propagation are controlled by the same mechanism (i.e. the shear mode), the reported defect size corresponds to the biggest defect observed on the failure surface.

Firstly, it can be seen that the defect size related to the first mechanism is larger than the one corresponding to the second mechanism and that a defect size $\sqrt{area}$ of 450 μm defines the boundary between the two mechanisms. In addition, it shows a slight increase in the stress level corresponding to the final step: for the first mechanism (Fig. 24a), at $\tau_{xy,a} = 70\,\text{MPa}$, 80% of specimens failed while for the second mechanism (Fig. 24b), 80% specimens survived. Hence, the defect size threshold of 450 μm can be considered as the critical defect size below which defects have negligible influence on the pure torsion fatigue strength. It is important to note that this threshold value is the same order of magnitude as the average grain area square root $\sqrt{area}_{average}$ in alloy C which is $\sqrt{area}_{average} = D_{e,average} \cdot \sqrt{\pi}/2 \approx 411\,\mu m$ (see Fig. 5). This value is supposed to be similar to that for alloy B.

7. Conclusions

The principal objective of this work was to better understand the HCF behaviour of the cast aluminium alloys under various uniaxial and multiaxial loading modes with a load ratio of $R = -1$. Three different cast aluminium alloys were investigated. These materials were fabricated by different casting processes (gravity die cast, lost foam cast) and subject to different heat treatments (T7, HIP). These different processes lead to three very different defect size distributions for the three alloys investigated:

- The characterisation of the HCF damage mechanisms shows very different crack initiation as well as crack propagation mechanisms, depending on loading modes.
- An investigation of PSB formation highlights the role of the aluminium matrix (via the crystallographic orientation, the precipitation hardening level and the SDAS) and the role of silicon particles for pure torsion load at $R = -1$.
- Via the investigation of the pore at the origin of the principal fatigue crack, it was shown that (a) the small crack effect is significant for natural fatigue cracks and (b) pores have less
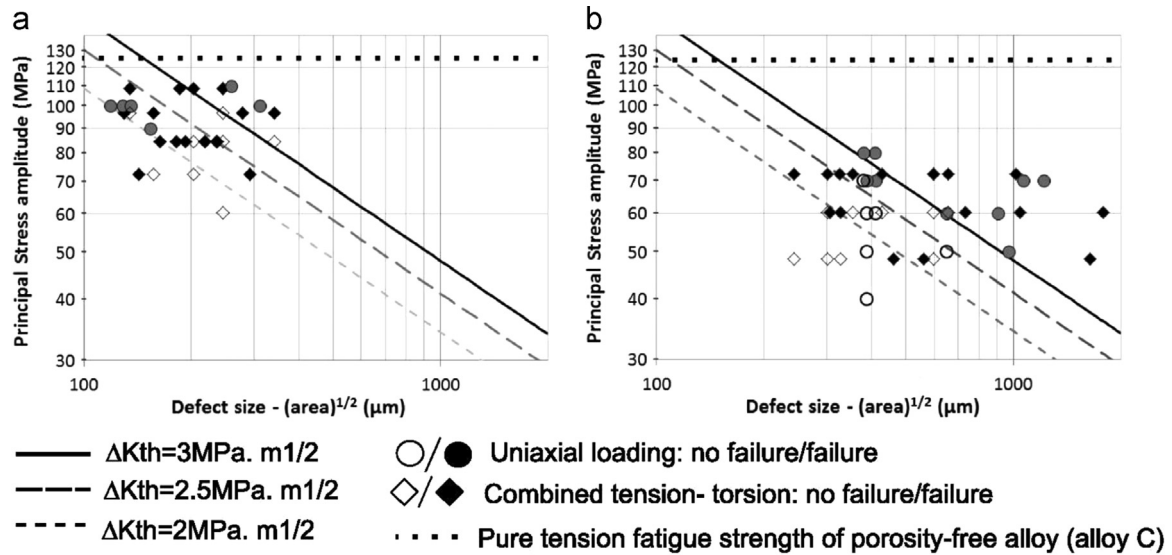
Fig. 23. Experimentally determined fatigue strengths as a function of the experimentally determined defect size for alloys A (a) and B (b) in uniaxial and combined tension–torsion load.
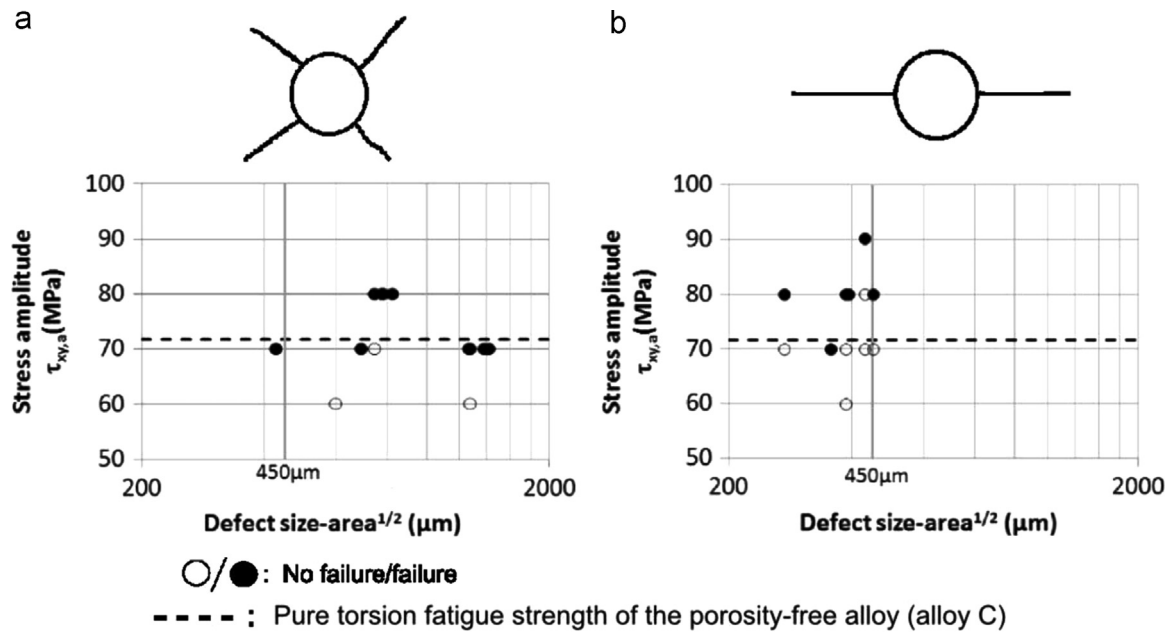

Fig. 24. Experimentally determined fatigue strengths as a function of the experimentally determined defect size for alloy B in pure torsional loads: (a) the first fatigue mechanism related to the crack propagation from pores in opening mode; (b) the second mechanism related to crack initiation from PSB followed by crack propagation due to the shear modes.

influence on the pure torsion fatigue strength compared to tension–compression and combined tension–torsion loads.

References

[1] Imade Koutiri, Daniel Bellett, Franck Morel, Louis Augustins, Jérôme Adrien, High cycle fatigue damage mechanisms in cast aluminium subject to complex loads, Int. J. Fatigue 47 (0) (2013) 44–57.

[2] Q.G. Wang, D. Apelian, D.A. Lados, Fatigue behavior of a356–t6 aluminum cast alloys. Part i. Effect of casting defects, J. Light Metals 1 (1) (2001) 73–84.

[3] D.L. McDowell, K. Gall, M.F. Horstemeyer, J. Fan, Microstructure-based fatigue modeling of cast a356–t6 alloy, Eng. Fract. Mech. 70 (1) (2003) 49–80.

[4] J.-Y. Buffière, S. Savelli, P.H. Jouneau, E. Maire, R. Fougères, Experimental study of porosity and its relation to fatigue mechanisms of model al–si7–mg0.3 cast al alloys, Mater. Sci. Eng. A 316 (1–2) (2001) 115–126.

[5] Q.G. Wang, D. Apelian, D.A. Lados, Fatigue behavior of a356/357 aluminum cast alloys. Part {II}—effect of microstructural constituents, J. Light Metals 1 (1) (2001) 85–97.

[6] Redik, Sabine, Tauscher, Markus, Grün, Florian, Mechanisms of fatigue-crack initiation and their impact on fatigue life of alsi7 die-cast components, in: MATEC Web of Conferences, vol. 12, 2014, p. 03003.

[7] James M. Boileau, John E. Allison, The effect of solidification time and heat treatment on the fatigue properties of a cast 319 aluminum alloy, Metall. Mater. Trans. A 34 (9) (2003) 1807–1820.

[8] P. Mu, Y. Nadot, C. Nadot-Martin, A. Chabod, I. Serrano-Munoz, C. Verdu, Influence of casting defects on the fatigue behavior of cast aluminum as7g06–t6, Int. J. Fatigue 63 (0) (2014) 97–109.

[9] Y. Murakami, Effects of Small Defects and Nonmetallic Inclusions, Elsevier, 2002, ISBN 978-0-08-044064-4.

[10] Bruno Barlas, Etude du comportement et de lendommagement en fatigue dalliages daluminium de fonderie (Ph.D. thesis), Ecole des Mines de Paris,

2004.

[11] L. Ceschini, Alessandro Morri, Andrea Morri, A. Gamberini, S. Messieri, Correlation between ultimate tensile strength and solidification microstructure for the sand cast a357 aluminium alloy, Mater. Des. 30 (10) (2009) 4525–4531.

[12] Kyuhong Lee, Yong Nam Kwon, Sunghak Lee, Effects of eutectic silicon particles on tensile properties and fracture toughness of {A356} aluminum alloys fabricated by low-pressure-casting, casting-forging, and squeeze-casting processes, J. Alloys Compd. 461 (1-2) (2008) 532–541.

[13] M.J. Roy, Y. Nadot, C. Nadot-Martin, P.-G. Bardin, D.M. Maijer, Multiaxial Kitagawa analysis of a356–t6, Int. J. Fatigue 33 (6) (2011) 823–832.

[14] M. Roy, Y. Nadot, D.M. Maijer, G. Benoit, Multiaxial fatigue behaviour of a356–t6, Fatigue Fract. Eng. Mater. Struct. 35 (12) (2012) 1148–1159.

[15] Y. Nadot, A. Chabaud, I. Serrano Mura, P. Mu, C. Verdu, J.Y. Buffière, P. Emile, C. Richard, L. Anssems, Influence of defect on the fatigue behaviour of as7g06t6 aeronautical alloy (ideffaar), in: The 2nd International Symposium on Fatigue Design and Material Defects, SF2M 06, 2014.

[16] M.J. Caton, J.W. Jones, H. Mayer, S. Stanzl-Tschegg, J.E. Allison, Demonstration of an endurance limit in cast 319 aluminum, Metall. Mater. Trans. A 34 (11) (2003) 33–41.

[17] M.J. Caton, J.W. Jones, J.E. Allison, The influence of heat treatment and solidification time on the behavior of small-fatigue-cracks in a cast aluminum alloy, Mater. Sci. Eng. A 314 (1–2) (2001) 81–85.

[18] Kwai S Chan, Peggy Jones, Qigui Wang, Fatigue crack growth and fracture paths in sand cast {B319} and {A356} aluminum alloys, Mater. Sci. Eng. A 341 (1–2) (2003) 18–34.

[19] B. Skallerud, T. Iveland, G. Härkegård, Fatigue life assessment of aluminum alloys with casting defects, Eng. Fract. Mech. 44 (6) (1993) 857–874.

[20] Y.X. Gao, J.Z. Yi, P.D. Lee, T.C. Lindley, A micro-cell model of the effect of microstructure and defects on fatigue resistance in cast aluminum alloys, Acta Mater. 52 (19) (2004) 5435–5449.

[21] Jinghong Fan, David L. McDowell, Mark F. Horstemeyer, Ken Gall, Cyclic plasticity at pores and inclusions in cast Al–Si alloys, Eng. Fract. Mech. 70 (10) (2003) 1281–1302.

[22] Lei Zeng, Junji Sakamoto, Atsushi Fujii, Hiroshi Noguchi, Role of eutectic silicon particles in fatigue crack initiation and propagation and fatigue strength characteristics of cast aluminum alloy {A356}, Eng. Fract. Mech. 115 (2014) 1–12.

[23] Imade Koutiri, Effet des fortes contraintes hydrostatiques sur la tenue en fatigue des matériaux métalliques (Ph.D. thesis), ENSAM, 2011.

[24] Komlan Agbessi, Approches expérimentales et multi-échelles des processus d'amorçage de fissures en fatigue sous chargements complexes (Ph.D. thesis), 2013. Thse de doctorat dirigée par Saintier, Nicolas Mécanique-matériaux Paris, ENSAM 2013.

[25] C. Robert, N. Saintier, T. Palin-Luc, F. Morel, Micro-mechanical modelling of high cycle fatigue behaviour of metals under multiaxial loads, Mech. Mater. 55 (0) (2012) 112–129.

[26] Stefanie Stanzl-Tschegg, Hael Mughrabi, Bernd Schoenbauer, Life time and cyclic slip of copper in the {VHCF} regime, Int. J. Fatigue 29(911) (2007) 2050–2059. Fatigue Damage of Structural Materials {VI} The Sixth International Conference on Fatigue Damage of Structural Materials.

[27] Pierre Osmond, Etude du vieillissement à chaud des alliages d'aluminium pour culasses diesel et prise en compte dans le dimensionnement (Ph.D. thesis), Mines ParisTech, 2010.

[28] S. Dezecot, M. Brochu, Microstructural characterization and high cycle fatigue behavior of investment cast {A357} aluminum alloy, Int. J. Fatigue 77 (2015) 154–159.

[29] Mohamed Iben Houria, Yves Nadot, Raouf Fathallah, Matthew Roy, Daan M. Maijer, Influence of casting defect and {SDAS} on the multiaxial fatigue behaviour of a356–t6 alloy including mean stress effect, Int. J. Fatigue 80, 2015, 90-102.

[30] D.C. Maxwell, T. Nicholas, A rapid method for generation of a Haigh diagram for high cycle fatigue, in: Fatigue and Fracture Mechanics, ASTM Special Technical Publication, STP, vol. 29, ASTM, West conshohocken, 1999, pp. 626–641.

[31] M.J. Couper, J.R. Griffiths, Effects of crack closure and mean stress on the threshold stress intensity factor for fatigue of an aluminium casting alloy, Fatigue Fract. Eng. Mater. Struct. 13 (6) (1990) 615–624.